

Article

Hydrogen Storage Properties of Economical Graphene Materials Modified by Non-Precious Metal Nickel and Low-Content Palladium

Yiwen Chen ^{1,2,†}, Habibullah ^{3,†}, Guanghui Xia ³, Chaonan Jin ³, Yao Wang ^{4,5}, Yigang Yan ^{4,5,6} ,
Yungui Chen ^{4,5,6}, Xiufang Gong ^{1,2,*}, Yuqiu Lai ^{1,2} and Chaoling Wu ^{3,4,5,*}

- ¹ State Key Laboratory of Clean and Efficient Turbomachinery Power Equipment, Deyang 618000, China; chenyiwenac@163.com (Y.C.); laiyuqiu2020@163.com (Y.L.)
- ² Dongfang Electric Corporation Dongfang Turbine Co., Ltd., Deyang 618000, China
- ³ College of Materials Science and Engineering, Sichuan University, Chengdu 610064, China; habibullah@stu.scu.edu.cn (H.); xiagh1994@163.com (G.X.); jinchaonnan@163.com (C.J.)
- ⁴ Engineering Research Center of Alternative Energy Materials & Devices, Ministry of Education, Chengdu 610064, China; wangyao516@scu.edu.cn (Y.W.); yigang.yan@scu.edu.cn (Y.Y.); chenYungui@scu.edu.cn (Y.C.)
- ⁵ Institute of New Energy and Low-Carbon Technology, Sichuan University, Chengdu 610065, China
- ⁶ Technology Innovation Center of Hydrogen Storage-Transportation and Fueling Equipments for State Market Regulation, Chengdu 610100, China
- * Correspondence: gongxiufang@dongfang.com (X.G.); wuchaoling@scu.edu.cn (C.W.)
- † These authors contributed equally to this work.

Abstract: Ni/Pd co-modified graphene hydrogen storage materials were successfully prepared by a solvothermal method using NiCl₂·6H₂O and Pd(OAc)₂ and reduced graphene oxide (rGO). By adjusting the hydrothermal temperature, Pd–Ni is successfully alloyed, and the size of the obtained nanoparticles is uniform. The electronic structure of Pd was changed by alloying, and the center of the D-band moved down, which promoted the adsorption of hydrogen. The NiPd-rGO-180 sample, in which 180 represents the solvothermal temperature in centigrade (°C), has the highest hydrogen storage capacity of 2.65 wt% at a moderate condition (RT/4MPa). The excellent hydrogen storage performance benefits from the synergistic hydrogen spillover effect of Pd–Ni bimetal. The calculated hydrogen adsorption energies of Ni₂Pd₂-rGO are within the ideal range (−0.20 to −0.60 eV) of hydrogen ads/desorption; however, the introduction of substrate defects and the cluster orientation alter the hydrogen adsorption energy. This work provides an effective reference for the design and optimization of carbon-based hydrogen storage materials.

Keywords: NiPd; graphene; carbon-based hydrogen storage; hydrogen adsorption



Citation: Chen, Y.; Habibullah; Xia, G.; Jin, C.; Wang, Y.; Yan, Y.; Chen, Y.; Gong, X.; Lai, Y.; Wu, C. Hydrogen Storage Properties of Economical Graphene Materials Modified by Non-Precious Metal Nickel and Low-Content Palladium. *Inorganics* **2023**, *11*, 251. <https://doi.org/10.3390/inorganics11060251>

Academic Editor: Hicham Idriss

Received: 18 May 2023

Revised: 2 June 2023

Accepted: 6 June 2023

Published: 8 June 2023



Copyright: © 2023 by the authors. Licensee MDPI, Basel, Switzerland. This article is an open access article distributed under the terms and conditions of the Creative Commons Attribution (CC BY) license (<https://creativecommons.org/licenses/by/4.0/>).

1. Introduction

Energy plays a crucial role in driving economic prosperity for nations worldwide. With the rapid growth of the population and evolving lifestyles, global energy demands continue to expand. Simultaneously, environmental concerns and the rapid depletion of resources have become alarming challenges. Fossil fuel consumption has notably contributed to environmental degradation, intensifying the need for clean and sustainable energy sources. In this context, hydrogen emerges as a promising solution to meet the growing energy requirements [1–3]. As an ecofriendly energy carrier, hydrogen offers a range of advantages, including a high gravimetric energy density, zero emissions, and a renewable nature. Its environmentally benign characteristics position it as a clean energy transporter [4]. With its immense potential, hydrogen is expected to serve as a highly efficient alternative fuel with diverse applications in the future. However, the development of highly efficient and safe hydrogen transportation and storage technologies remains a subject of discussion

and demonstration. Currently, high-pressure compressed hydrogen is the most commonly employed storage technology, although concerns regarding safety persist. Among the three primary techniques for hydrogen storage, namely compressed gas, cryogenic liquid, and solid-state storage, only the former two methods have commercialized. Nevertheless, the cost-effectiveness and safety considerations of hydrogen storage have led to significant research efforts focusing on solid-state storage through the adsorption and/or absorption of various materials and alloys [5,6]. The growing development of the new energy automotive sector has spurred numerous studies on secure hydrogen storage. Porous materials, including zeolites, metal-organic frameworks (MOFs), covalent organic frameworks (COFs), and carbon-based materials (such as fullerenes, nanotubes and graphene), have received considerable attention [7]. However, the low hydrogen storage capacity of zeolites and porous silica, along with the low operating temperature (77K) of MOFs and COFs, pose disadvantages for hydrogen storage [8,9]. As a result, 2D carbonaceous materials [10], particularly graphene [11,12], have emerged as a topic of significant interest in the field of hydrogen storage materials. Graphene offers exceptional specific surface area, structural stability, lightweight properties and rapid adsorption kinetics [13–15]. Despite the relatively low hydrogen storage capacity of pure graphene (<1 wt% at room temperature), which falls short of the U.S. Department of Energy (DOE) target of 5.5 wt% for onboard applications by 2025 [16], it remains a subject of exploration and optimization for hydrogen storage purposes. Some researchers confirmed that there is an increment in the hydrogen storage capacity of graphene after being modified by metal atoms, clusters, or nanoparticles. Palladium, platinum, and other precious metals have been widely studied and used to enhance the hydrogen storage capacity of carbon-based materials owing to the hydrogen spillover effect [17–19]. However, the high cost has inhibited the large-scale industrial application of these precious metals. The spillover process in hydrogen storage involves the dissociation of hydrogen molecules on the catalyst, migration of hydrogen atoms from the catalyst to the substrate, and diffusion of hydrogen atoms on the substrate surface. However, certain pure transition metal-decorated graphene materials face limitations due to a high energy barrier. For instance, Psfogiannakis et al. [20] reported a migration barrier of 2.6 eV from the Pt₄ cluster to graphene. This high migration barrier hampers the efficient and thermodynamically favorable transfer of hydrogen atoms from the catalyst to the carbon receptor, thereby impeding the spillover rate of hydrogen.

To reduce the reliance on precious metals such as Pd, the formation of Pd-based alloys has emerged as an effective strategy. The introduction of alloying elements can alter the hydrogen spillover effect and consequently modify hydrogen storage capacity. Guo et al. conducted research on the highest occupied molecular orbital (HOMO) of Penta-Graphene (PG) decorated with Ni₄, Pd₄, and Ni₂Pd₂. Their findings revealed that the orbit of Ni overlaps with that of Pd, resulting in a decrease in the electric field of the Ni₂Pd₂ cluster compared to Ni₄ and Pd₄. This decrease leads to a reduction in hydrogen adsorption energy [21]. In another study by Wu et al., a systematic comparison of the properties of Pd₆Ni₄ and Pd₄Ni₆ was conducted [22]. It was observed that the migration of electrons between Pd and Ni caused the D-band center of Pd to shift downward. Our previous research demonstrated that P doping improves the electronic structure of Pd, resulting in a downward shift of the D-band center. This, in turn, weakens the adsorption energy of materials for H₂, lowers the diffusion energy barrier of H atoms, and promotes hydrogen spillover, thereby enhancing hydrogen absorption and desorption capacity [23]. Based on this understanding, the design and synthesis of Pd–Ni alloys hold promise for improving hydrogen storage performance by adjusting the D-band center.

Moreover, despite extensive research efforts in the field of hydrogen storage, the development of efficient onboard hydrogen storage systems still poses significant scientific and technological challenges. To address this issue, we have conducted a comprehensive investigation, taking into account previous experimental and computational studies towards the development of an economically viable graphene-based hydrogen storage material. In our study, we successfully synthesized the material using a solvothermal method, wherein

palladium (Pd) was incorporated to partially replace nickel (Ni). Notably, the utilization of ethylene glycol as the hydrothermal solvent resulted in the coexistence of Ni and Pd in the final material. Concurrently, some Pd atoms infiltrated the Ni lattice, forming a NiPd alloy. Our findings reveal that the NiPd-rGO material exhibits a remarkable maximum hydrogen storage capacity of 2.65 wt% under mild conditions, specifically at 4 MPa and 298 K.

2. Material Preparation

2.1. Obtaining NiPd-rGO at Different Hydrothermal Temperatures

The experimental procedure commenced by dispersing 100 mg of graphene oxide (GO) powder in a mixed solution comprising 30 mL of ethylene glycol and 30 mL of de-ionized water. To this mixture, 78 mg of Pd(OAc)₂ and 150 mg of NiCl₂·6H₂O were added. The pH of the solution was adjusted to 12–13 using an appropriate amount of KOH. The resulting solution, containing the dispersed components, was transferred to a 100 mL Teflon-lined reaction kettle, sealed, and placed in an oven. The temperature of the oven was sequentially raised to 160 °C, 180 °C and 200 °C, allowing the hydrothermal reaction to proceed for 12 h at each temperature. After the hydrothermal reaction was completed, the resulting black solution was left undisturbed for 6 h. The supernatant was carefully decanted, and the remaining material was subjected to repeated washing with deionized water using suction filtration until the pH reached a neutral level. Subsequently, the material was freeze-dried for 12 h, resulting in the formation of a black powder. To further enhance the material, the obtained black powders underwent a heat treatment process at 500 °C for 1 h under a 10% H₂/Ar atmosphere, employing a heating rate of 5 °C/min. This final treatment led to the formation of NiPd-rGO, the desired product of the synthesis process.

2.2. Computational Methodology

For this study, a Ni₂Pd₂ cluster and a graphene slab consisting of sixty carbon atoms, along with a single attached oxygen atom (rGO), were employed. To prevent interactions between neighboring layers, a vacuum layer with a thickness of 15 Å was added in the Z-direction. The formation of single-vacancy-reduced graphene oxide (SVrGO) was achieved by removing a carbon atom from the center of the graphene sheet and attaching an oxygen atom to the resulting vacancy, resulting in a graphene sheet with fifty-nine atoms. Subsequently, the structure was optimized to attain a stable configuration. Density Functional Theory (DFT) was employed as the computational method in this study. It allowed for the calculation of important parameters such as the binding energy between the Ni₂Pd₂ cluster and SVrGO, as well as the adsorption energy of hydrogen (H₂) on the composite material. Vienna Ab initio Simulation Package (VASP) was used to perform the calculations. The exchange and correlation interactions were described using generalized gradient approximation (GGA) in the form of the Perdew–Burke–Ernzerhof (PBE) functional. The calculations used a Brillouin region of 5 × 5 × 1 as the k-point value, and the geometry optimization structure was obtained by relaxation until the force on each atom was less than 0.02 eV/Å, and the convergence criterion for energy was chosen as 1 × 10^{−4} eV. The cutoff energy was 450 eV, and all calculations considered spin polarization. The converged bond length for pristine graphene was determined to be 1.42 Å which shows that all the parameters used in this calculation are valid. The study employed an equation to determine the adsorption energy of the cluster and slab:

$$E_{(B)} = E_{(Cluster+substrate)} - E_{(substrate)} - E_{(cluster)} \quad (1)$$

where $E_{(B)}$ is the binding energy, $E_{(cluster+substrate)}$ is the total energy of a system, $E_{(substrate)}$ is the total energy of slab and $E_{(cluster)}$ is the total energy of cluster. The following equation has been utilized for the adsorption energy of the H₂ molecule, taking into account the vibration effect for a gas phase only, as it is nearly negligible for a solid system.

$$E_{(ads)} = \left(E_{(H_2+Cluster+substrate)} + \Delta ZPE \right) - E_{(cluster+substrate)} - \left(E_{(H_2)} + \Delta ZPE \right) \quad (2)$$

where $E_{(ads)}$ is the H_2 adsorption energy, $E_{(H_2+cluster+substrate)}$ is the total energy of a system, $E_{(cluster+substrate)}$ is the total energy of the cluster-decorated substrate, $E_{(H_2)}$ is the total energy of a single H_2 molecule and ΔZPE is the zero-point energy correction.

3. Results and Discussion

Figure 1 illustrates the X-ray diffraction (XRD) patterns obtained from the NiPd-rGO-X ($X = 160, 180, 200$ °C) samples, synthesized at different hydrothermal temperatures. A comparison with standard PDF cards allowed for the identification of a biphasic structure within the material, indicating the coexistence of Pd and Ni phases. The peaks observed at 40.2° , 46.8° , 68.3° , 82.4° and 86.9° correspond to Pd (111), Pd (200), Pd (220), Pd (311) and Pd (222), respectively, as per the PDF database. Of particular interest, the peaks associated with Ni (PDF#70-1849) exhibited a noticeable shift towards lower angles, implying the incorporation of Pd atoms into the Ni lattice, thereby forming a NiPd alloy [24]. This observation is evident from the shift of the Ni (111) diffraction peak towards smaller angles, indicating an expansion of the nickel unit cell due to alloying with palladium. The XRD peaks change with the variation in temperature. At 160 °C, the material predominantly exhibits a split phase composed of palladium and nickel. The XRD analysis indicates that the nickel content within the palladium lattice is relatively low, and correspondingly, the palladium content within the nickel lattice is also relatively small. As the temperature is increased to 180 °C, there is an augmentation in the quantity of palladium integrated into the nickel lattice, leading to the formation of a greater number of palladium–nickel alloys with nickel as the primary phase. Subsequently, at 200 °C, the amount of nickel incorporated into the palladium lattice increases, resulting in the transformation of the material into a palladium–nickel alloy with palladium as the principal phase. Moreover, the shift in the position of the XRD peaks can serve as evidence. At 160 °C, the phase exhibits closer proximity to our palladium and nickel composition. At 180 °C, the palladium content within the nickel lattice notably increases, leading to a greater shift in the peak position. Finally, at 200 °C, the position of the nickel peak shifts in the opposite direction, while the peak shift of palladium becomes more pronounced. This finding suggests a higher proportion of Ni alloyed with Pd in the sample synthesized at 180 °C, indicating that 180 °C may be the optimum hydrothermal temperature for the synthesis of NiPd. The higher proportion of Ni in the NiPd alloy synthesized at 180 °C is particularly significant as Ni is more cost-effective than Pd. Therefore, the increased proportion of Ni offers a promising avenue for achieving a cost-effective hydrogen storage material in the NiPd alloy synthesized at 180 °C.

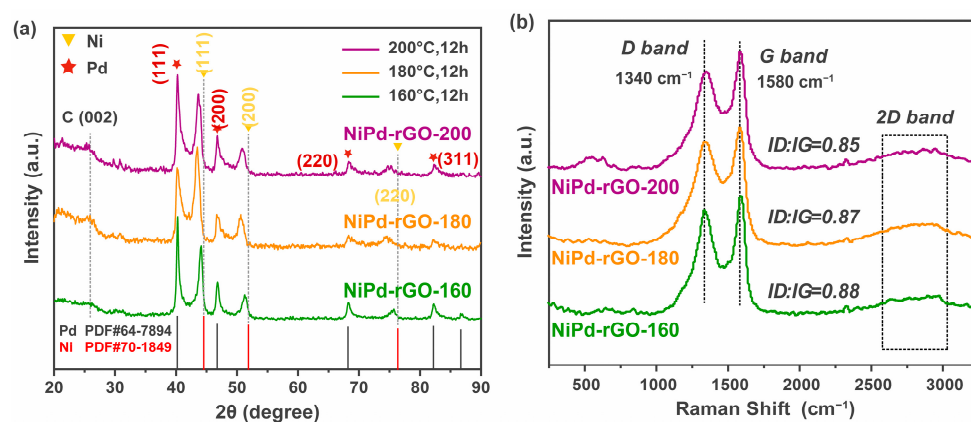


Figure 1. (a) XRD patterns, (b) Raman spectra of NiPd-rGO-X ($X = 160, 180, 200$ in °C) prepared at different hydrothermal temperatures.

In order to investigate the presence of defects within the materials, Raman spectroscopy was employed to analyze the NiPd-rGO-X samples (where X represents the hydrothermal temperature of $160, 180,$ and 200 °C), as illustrated in Figure 1b. The obtained

spectra for all three samples exhibited the presence of the D-band and G-band. The D-band, positioned at 1340 cm^{-1} , corresponds to the disordered hybridization of sp^2 [25], while the G-band, observed at 1580 cm^{-1} , is associated with the stretching of the C-C bond within the graphene material. Furthermore, upon conducting calculations, it was discovered that the NiPd-rGO-160 sample exhibited the highest I_D/I_G ratio, measuring 0.88. It is worth noting that the I_D/I_G ratio tends to decrease as the hydrothermal temperature increases. Consequently, the NiPd-rGO-200 sample displayed the lowest I_D/I_G ratio, amounting to 0.85.

To examine the distribution of nanoparticles on the materials, field emission scanning microscopy (FESEM) was utilized to investigate the morphologies of the NiPd-rGO-X samples. The findings, depicted in Figure 2, demonstrate a uniform distribution of NiPd nanoparticles on the graphene surface. The grain size of these nanoparticles ranges from 5 to 45 nm, exhibiting a normal distribution pattern. A detailed analysis of Figure 2 indicates that as the hydrothermal temperature increases, the size of the nanoparticles loaded on the graphene surface tends to decrease. However, it is worth noting that beyond a temperature of $180\text{ }^\circ\text{C}$, the size variations become insignificant, thereby further corroborating that $180\text{ }^\circ\text{C}$ represents the optimal hydrothermal temperature. Moreover, an interesting observation is made with the increase in hydrothermal temperature, wherein some larger particles present in the NiPd-rGO-160 sample disappear. In the NiPd-rGO-200 sample, the particle size distribution falls within the range of 5–40 nm, exhibiting a narrower distribution compared to that observed in NiPd-rGO-160.

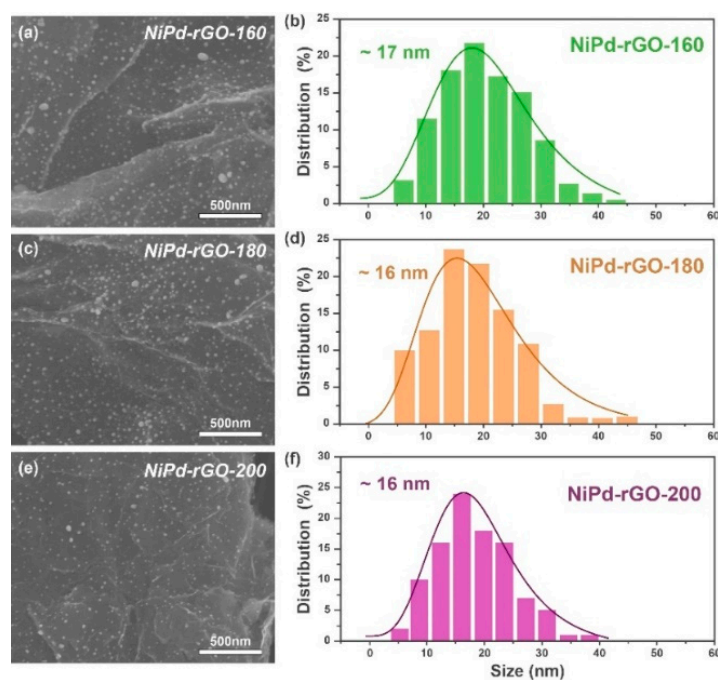


Figure 2. SEM images ((a) = NiPd-rGO-160, (c) = NiPd-rGO-180, (e) = NiPd-rGO-200) and particle size distribution ((b) = NiPd-rGO-160, (d) = NiPd-rGO-180, (f) = NiPd-rGO-200) of NiPd-rGO-X (X = 160, 180, 200 in $^\circ\text{C}$) prepared at different hydrothermal temperatures.

The specific surface area and pore size distribution of the NiPd-rGO-X material were determined through N_2 isothermal adsorption–desorption tests conducted at a temperature of 77 K . Figure 3a,b display the N_2 adsorption–desorption isotherms and pore size distribution curves of NiPd-rGO-X, respectively. It is evident that the N_2 adsorption–desorption isotherms of all three samples exhibit the characteristic features of type-IV adsorption isotherms, suggesting the presence of a mesoporous structure within the material. The observed hysteresis in the isotherms further supports the existence of mesopores. Among the samples, NiPd-rGO-200 exhibited the highest specific surface area, measuring $137.89\text{ m}^2/\text{g}$.

It is noteworthy that the specific surface area demonstrated a decreasing trend as the hydrothermal temperature was reduced, which could be attributed to the exfoliation of graphene layers at higher temperatures. The average pore diameter of NiPd-rGO-X was determined to be approximately 2.5 nm, indicating a similarity in the pore structure among the three samples. Nevertheless, the pore volume diminished with decreasing hydrothermal temperature, consistent with the variation in specific surface area, thus suggesting a correlation between pore volume and surface area.

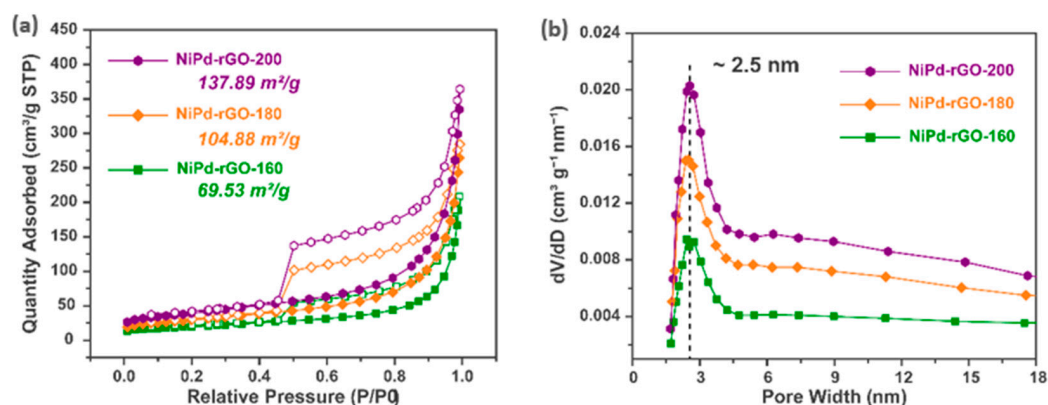


Figure 3. (a) N₂ isotherm adsorption–desorption curves, (b) pore size distribution of NiPd-rGO-X (X = 160, 180, 200 in °C) prepared at different hydrothermal temperatures.

The X-ray photoelectron spectroscopy (XPS) technique was utilized to investigate the surface state of the samples in detail. Figure 4 showcases the XPS spectrum of NiPd-rGO-X. Upon analyzing the survey spectra, distinct peaks corresponding to C, O, Pd and Ni are observed. In the 1s spectrogram of C, the peaks at 284 eV, 284.8 eV and 286.3 eV correspond to the C=C bond, C-O bond and C=O bond, respectively. These peaks indicate the presence of incompletely reduced oxygen-containing groups in rGO, thus reflecting its surface composition [26]. Moving on to Figure 4c, it is observed that the peaks at 335.1 eV and 340.2 eV correspond to the 3d_{5/2} orbital and 3d_{3/2} orbital of Pd⁽⁰⁾, respectively. Additionally, the peaks at 336 eV and 341.5 eV correspond to the 3d_{5/2} orbital and 3d_{3/2} orbital of Pd^(II), respectively. This indicates the coexistence of Pd in different oxidation states, suggesting the formation of PdO [27]. Notably, in comparison to Pd-rGO, the peak of Ni-Pd-rGO shifts towards a higher binding energy, indicating a change in the chemical state of the Pd atom. This forward movement suggests electron transfer from Pd to Ni after alloying, leading to a decrease in the center of the D-band [28]. The downward shift of the D-band center corresponds to a reduction in the adsorption of H by metals, thereby promoting hydrogen spillover and improving the hydrogen storage performance of the materials. Lastly, as depicted in Figure 4d, the peaks at 853.0 eV and 871.1 eV are associated with Ni, while the peaks at 855.5 eV and 873.1 eV are attributed to Ni²⁺, indicating the oxidation of Ni on the surface of the sample.

The hydrogen adsorption kinetic curves of NiPd-rGO-X at a pressure of 4 MPa and temperature of 298 K are illustrated in Figure 4a. The measured hydrogen storage capacities of the NiPd-rGO-160, NiPd-rGO-180, and NiPd-rGO-200 samples are 2.60 wt%, 2.65 wt% and 2.63 wt%, respectively, indicating their close proximity as shown in Figure 5. The marginally higher hydrogen storage capacity observed in the NiPd-rGO-180 sample can be attributed to the enhanced alloying degree of NiPd, resulting in a more efficient hydrogen spillover effect compared to the Pd and Ni single phases. Notably, the NiPd-rGO-180 material exhibits the highest hydrogen storage capacity (2.65 wt%) among the Ni-rGO, Pd-rGO and NiPd-rGO materials. This remarkable improvement is ascribed to the synergistic effect of rGO and PdNi, which alters the diffusion behavior of hydrogen molecules within the composites. Specifically, the PdNi alloy particles act as activation centers, facilitating the decomposition of hydrogen molecules into hydrogen atoms. These atoms are then

stored within the surface defects of graphene, thereby enhancing the overall hydrogen storage capacity of the material. This phenomenon is consistent with the findings of other researchers, who have reported on the higher affinity of defects for hydrogen adsorption from other surface sites [29,30].

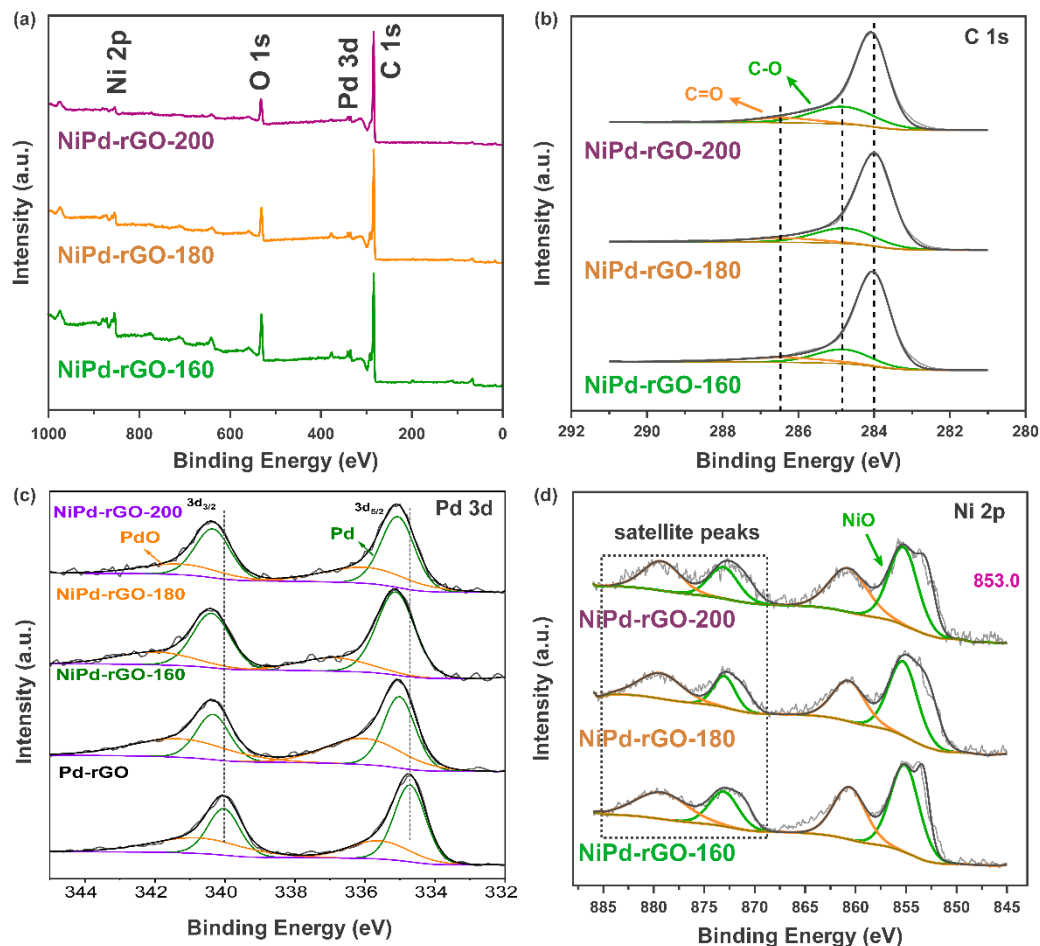


Figure 4. XPS spectra of NiPd-rGO-X (X = 160, 180, 200 in °C) prepared at different hydrothermal temperatures: (a) survey spectra, (b) C 1s, (c) Pd 3d and (d) Ni 2p orbitals.

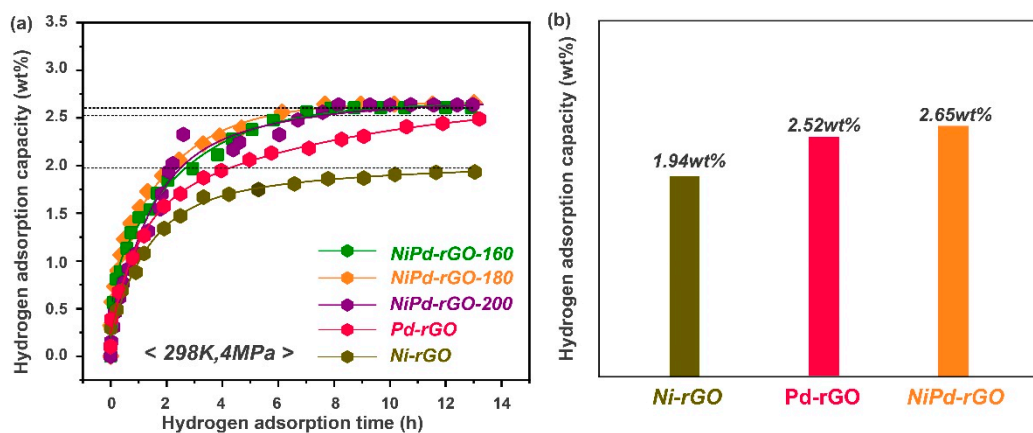


Figure 5. (a) Hydrogen adsorption kinetic curves and (b) hydrogen storage capacity at 4 MPa/298 K of different samples.

Following the optimization of the graphene slabs, as well as Ni₂Pd₂ clusters, the cluster was placed onto rGO and SVrGO, where the cluster of the Ni₂Pd₂ was tested in

different orientations and is presented in Figure 6. To evaluate the stability of Ni_2Pd_2 on different graphene surfaces, the binding energies were determined using Equation (1), and the findings of our study suggest that the cluster is supported on rGO (with no defects) with three different orientations as shown in the following: Figure 6a, Pd atoms attached to carbon having a binding energy of -1.03 eV; Figure 6b, Ni atoms attached to carbon having a binding energy of -2.60 eV, which is higher than the former case due to bonding of the oxygen atom with the Ni atom; and Figure 6c, Pd and Ni atoms attached to carbon having a binding energy of -1.1 eV, which do not seem to be suitable materials for hydrogen storage. This is attributed to lower binding energy which can cause metal atoms agglomeration which reduces the hydrogen storage capacity. As we know, during metal–metal interaction, metal atoms tend to cluster together, resulting in larger clusters rather than being evenly dispersed on the substrate. This clustering phenomenon is much stronger than the cluster–substrate interaction, which minimizes the efficiency of hydrogen molecule interaction.

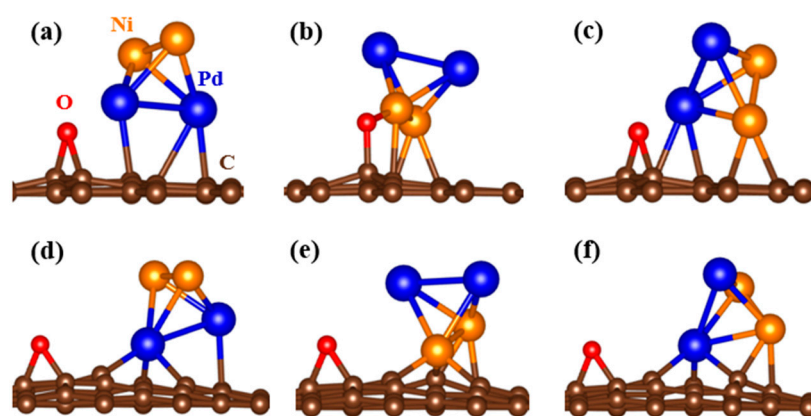


Figure 6. The side view of optimized structures of Ni_2Pd_2 cluster supported on rGO (a–c) and SVrGO (d–f) substrates.

Moreover, the desorption of metal–hydrogen complexes competes with the desorption of H_2 from pure graphene, further hindering the overall hydrogen storage process [31]. To address these issues, defect modifications have been employed as techniques to enhance the interaction between graphene and hydrogen molecules. Conversely, the binding energies of Ni_2Pd_2 supported on SVrGO with three different orientations are shown in the following: Figure 6d, Pd atoms attached to carbon vacancy having a binding energy of -4.72 eV; Figure 6e, Ni atoms attached to carbon having a binding energy of -6.61 eV; and, finally, Figure 6f, Pd and Ni atoms attached to carbon having a binding energy of -5.17 eV. Therefore, these substrates are not conducive to clustering. The results of our study also highlight the significance of defects in the graphene slab, as they significantly increase the binding energy between the transition metal cluster and the substrate. Our calculations indicate that the binding energy is approximately four times higher with the introduction of defects, which is consistent with previous findings reported by Kim et al. [32]. This increase in binding energy not only enhances the hydrogen storage capacity of the system but also addresses the challenge of complex hydride desorption during hydrogen molecule release [31]. By effectively increasing the binding energy, the presence of defects in the graphene structure offers a promising solution for improving hydrogen storage capabilities and overcoming the issue of complex hydride desorption.

In order to calculate the adsorption energy of the H_2 molecule, Equation (2) was applied which considers the vibration effect only for the gas phase since it is almost negligible for a solid system. The optimized structures and corresponding calculated adsorption energies of single H_2 molecules adsorbed on Ni_2Pd_2 -rGO and Ni_2Pd_2 -SVrGO at different positions within the orientation of the cluster are illustrated in Figure 7. The adsorption energies with negative values in Figure 7 indicate favorable adsorption, as they

signify the attraction of H₂ molecules toward the cluster. Upon structural optimization, the H-H bond underwent relaxation, resulting in bond lengths ranging from 0.83 Å to 0.88 Å, and adsorbed H₂ molecules exhibited an increase in bond length on all materials as compared to the free H₂ bond length of 0.75 Å. However, when compared to an isolated H₂ molecule, the stretching of the H-H bond length was found to be minimal, with a difference of less than 0.3 Å [33], indicating non-dissociative chemisorption or “molecular” adsorption of H₂, with the association between the H₂ molecule and the Ni and Pd atoms resulting from Kubas-type interaction. Additionally, the bond length between Ni and H varies between 1.56 Å and 1.64 Å, and the bond length of Pd and H varies between 1.72 Å and 1.79 Å. As shown in Figure 7, it is observed that the adsorption energies are different from each other, which means that the orientation of the cluster and defects in the slabs alter the adsorption energy of the H₂ molecule. Successful hydrogen storage under ambient conditions requires an adsorption mechanism that falls between physical and chemical adsorption, with previous studies recommending an adsorption energy range of -0.20 to -0.60 eV [34], which is consistent with the adsorption energies observed in this study. All materials fall within this range except Figure 7(e, g), indicating their potential for hydrogen storage.

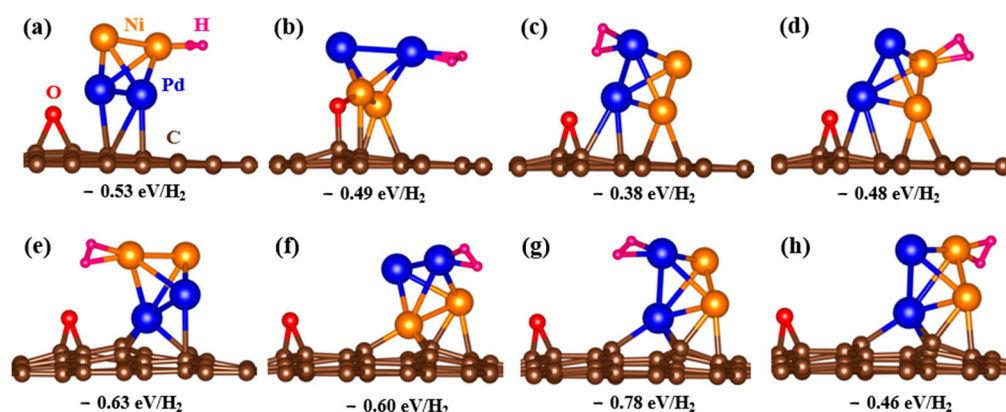


Figure 7. The side view of optimized structures of H₂ adsorbed on different sites on Ni₂Pd₂ cluster supported on rGO (a–d) and SVrGO (e–h) substrates.

4. Conclusions

In this study, we employed the hydrothermal method to synthesize NiPd-rGO, aiming to develop a novel hydrogen storage material with improved capacity at moderate operating conditions and reduced cost. The obtained material exhibited a higher hydrogen storage capacity of 2.65 wt% (at 4 MPa and 298 K) compared to its Ni-rGO and Pd-rGO counterparts. This enhanced capacity can be attributed to the synergistic effect between the alloy particles and rGO. The process of alloying induced changes in the electronic structure of Pd, leading to a decrease in the center of the D-band. Consequently, the adsorption of hydrogen on the metal surface weakened, promoting the hydrogen spillover effect. Additionally, we investigated the binding energies with different orientations. The range of binding energies was found to be -1.03 to -2.60 eV for Ni₂Pd₂-rGO and -4.72 to -6.61 eV for Ni₂Pd₂-SVrGO. These results indicate that the introduction of defects into the graphene substrate enhances the interaction between the supported cluster and the substrate, thereby improving the stability of the material and reducing the likelihood of transition metal atom agglomeration. The calculated adsorption energies fell within the ideal range of -0.20 to -0.60 eV, which is conducive to efficient hydrogen ad/desorption processes. Furthermore, the introduction of defects in the substrate and the orientation of the supported cluster were found to influence the hydrogen adsorption energy. These findings contribute to the advancement of hydrogen storage technologies and pave the way for the design and optimization of graphene-based materials with superior hydrogen storage properties.

Author Contributions: Conceptualization, Y.C. (Yungui Chen), X.G. and C.W.; Validation, G.X., C.J., Y.W., Y.Y., X.G., Y.L. and C.W.; Formal analysis, Y.C. (Yiwen Chen) and H.; Investigation, H., Y.W., X.G. and C.W.; Writing—original draft, Y.C. (Yiwen Chen) and H.; Writing—review & editing, Y.C. (Yiwen Chen), H., G.X., C.J., Y.Y. and Y.L.; Visualization, Y.W., X.G. and C.W.; Supervision, G.X. and C.J. All authors have read and agreed to the published version of the manuscript.

Funding: This research was funded by National Natural Science Foundation of China (U2030208, U2130208); National Key R&D Program of China (2022YFB3803700); State Key Laboratory of Clean and Efficient Turbomachinery Power Equipment (DECSKL202110); Fundamental Research Funds for Central Universities, China.

Data Availability Statement: No new data were created or analyzed in this study. Data sharing is not applicable to this article.

Conflicts of Interest: The authors declare no conflict of interest.

References

1. Shafiee, S.; Topal, E. When will fossil fuel reserves be diminished? *Energy Policy* **2009**, *37*, 181–189. [CrossRef]
2. Chakraborty, B.; Ray, P.; Garg, N.; Banerjee, S. High capacity reversible hydrogen storage in titanium doped 2D carbon allotrope Ψ -graphene: Density Functional Theory investigations. *Int. J. Hydrogen Energy* **2021**, *46*, 4154–4167. [CrossRef]
3. Li, H.-M.; Li, G.-X.; Li, L. Comparative investigation on combustion characteristics of ADN-based liquid propellants in inert gas and oxidizing gas atmospheres with resistive ignition method. *Fuel* **2023**, *334*, 126742. [CrossRef]
4. Midilli, A.; Ay, M.; Dincer, I.; Rosen, M.A. On hydrogen and hydrogen energy strategies I: Current status and needs. *Renew. Sustain. Energy Rev.* **2005**, *9*, 255–271. [CrossRef]
5. Liu, W.; Sun, L.; Li, Z.; Fujii, M.; Geng, Y.; Dong, L.; Fujita, T. Trends and future challenges in hydrogen production and storage research. *Environ. Sci. Pollut. Res.* **2020**, *27*, 31092–31104. [CrossRef] [PubMed]
6. Lijun, J. Expediting the Innovation and Application of Solid Hydrogen Storage Technology. *Engineering* **2021**, *7*, 731–733.
7. Sun, Y.; DeJaco, R.F.; Li, Z.; Tang, D.; Glante, S.; Sholl, D.S.; Colina, C.M.; Snurr, R.Q.; Thommes, M.; Hartmann, M.; et al. Fingerprinting diverse nanoporous materials for optimal hydrogen storage conditions using meta-learning. *Sci. Adv.* **2021**, *7*, eabg3983. [CrossRef]
8. Chen, Z.; Kirlikovali, K.O.; Idrees, K.B.; Wasson, M.C.; Farha, O.K. Porous materials for hydrogen storage. *Chem* **2022**, *8*, 693–716. [CrossRef]
9. Gor Bolen, M. Hydrogen Storage in Porous Silicon—A Review. *Silicon* **2023**. [CrossRef]
10. Guo, J.-H.; Li, S.-J.; Su, Y.; Chen, G. Theoretical study of hydrogen storage by spillover on porous carbon materials. *Int. J. Hydrogen Energy* **2020**, *45*, 25900–25911. [CrossRef]
11. Shiraz, H.G.; Tavakoli, O. Investigation of graphene-based systems for hydrogen storage. *Renew. Sustain. Energy Rev.* **2017**, *74*, 104–109. [CrossRef]
12. Wang, Y.; Meng, Z.; Liu, Y.; You, D.; Wu, K.; Lv, J.; Wang, X.; Deng, K.; Rao, D.; Lu, R. Lithium decoration of three dimensional boron-doped graphene frameworks for high-capacity hydrogen storage. *Appl. Phys. Lett.* **2015**, *106*, 063901. [CrossRef]
13. Luo, Z.; Fan, X.; Pan, R.; An, Y. A first-principles study of Sc-decorated graphene with pyridinic-N defects for hydrogen storage. *Int. J. Hydrogen Energy* **2017**, *42*, 3106–3113. [CrossRef]
14. Patchkovskii, S.; Tse, J.S.; Yurchenko, S.N.; Zhechkov, L.; Heine, T.; Seifert, G. Graphene nanostructures as tunable storage media for molecular hydrogen. *Proc. Natl. Acad. Sci. USA* **2005**, *102*, 10439–10444. [CrossRef] [PubMed]
15. Weizhi, T.; Ying, Z.; Yazhou, W.; Tong, L.; Hong, C. A study on the hydrogen storage performance of graphene-Pd(T)-graphene structure. *Int. J. Hydrogen Energy* **2020**, *45*, 12376–12383.
16. DOE Technical Targets for Onboard Hydrogen Storage for Light-Duty Vehicles. Available online: <https://www.energy.gov/eere/fuelcells/doe-technical-targets-onboard-hydrogen-storage-light-duty-vehicles> (accessed on 31 May 2023).
17. Xu, B.; Li, X.; Chen, Z.; Zhang, T.; Li, C. Pd@MIL-100(Fe) composite nanoparticles as efficient catalyst for reduction of 2/3/4-nitrophenol: Synergistic effect between Pd and MIL-100(Fe). *Microporous Mesoporous Mater.* **2018**, *255*, 1–6. [CrossRef]
18. Wan, W.C.; Zhang, R.Y.; Ma, M.Z.; Zhou, Y. Monolithic aerogel photocatalysts: A review. *J. Mater. Chem. A* **2018**, *6*, 754–775. [CrossRef]
19. Liu, D.; Xie, M.; Wang, C.; Liao, L.; Qiu, L.; Ma, J.; Huang, H.; Long, R.; Jiang, J.; Xiong, Y. Pd-Ag alloy hollow nanostructures with interatomic charge polarization for enhanced electrocatalytic formic acid oxidation. *Nano Res.* **2016**, *9*, 1590–1599. [CrossRef]
20. Psfogiannakis, G.M.; Froudakis, G.E. DFT Study of the Hydrogen Spillover Mechanism on Pt-Doped Graphite. *J. Phys. Chem. C* **2009**, *113*, 14908–14915. [CrossRef]
21. Guo, J.-H.; Li, X.-D.; Cheng, X.-L.; Liu, H.-Y.; Li, S.-J.; Chen, G. The theoretical study of the bimetallic Ni/Pd, Ni/Pt and Pt/Pd catalysts for hydrogen spillover on penta-graphene. *Int. J. Hydrogen Energy* **2018**, *43*, 19121–19129. [CrossRef]
22. Wu, S.-Y.; Chen, H.-T. Structure, Bonding, and Catalytic Properties of Defect Graphene Coordinated Pd-Ni Nanoparticles. *J. Phys. Chem. C* **2017**, *121*, 14668–14677. [CrossRef]

23. Jin, C.; Li, J.; Zhang, K.; Habibullah; Xia, G.; Wu, C.; Wang, Y.; Cen, W.; Chen, Y.; Yan, Y.; et al. Pd3P nanoparticles decorated P-doped graphene for high hydrogen storage capacity and stable hydrogen adsorption-desorption performance. *Nano Energy* **2022**, *99*, 107360. [[CrossRef](#)]
24. Chen, Z.; Zhang, J.; Zhang, Y.; Liu, Y.; Han, X.; Zhong, C.; Hu, W.; Deng, Y. NiO-induced synthesis of PdNi bimetallic hollow nanocrystals with enhanced electrocatalytic activities toward ethanol and formic acid oxidation. *Nano Energy* **2017**, *42*, 353–362. [[CrossRef](#)]
25. Reich, S.; Thomsen, C. Raman spectroscopy of graphite. *Philos. Trans. R. Soc. A Math. Phys. Eng. Sci.* **2004**, *362*, 2271–2288. [[CrossRef](#)]
26. Yang, G.; Chen, Y.; Zhou, Y.; Tang, Y.; Lu, T. Preparation of carbon-supported Pd-P catalyst with high content of element phosphorus and its electrocatalytic performance for formic acid oxidation. *Electrochem. Commun.* **2010**, *12*, 492–495. [[CrossRef](#)]
27. Qiu, B.; Li, Q.; Shen, B.; Xing, M.; Zhang, J. Stober-like method to synthesize ultradispersed Fe₃O₄ nanoparticles on graphene with excellent Photo-Fenton reaction and high-performance lithium storage. *Appl. Catal. B-Environ.* **2016**, *183*, 216–223. [[CrossRef](#)]
28. Belykh, L.B.; Sterenchuk, T.P.; Skripov, N.I.; Akimov, V.V.; Tauson, V.L.; Romanchenko, A.S.; Gvozdovskaia, K.L.; Sanzhieva, S.B.; Shmidt, F.K. Effect of the State of a Surface Layer on the Properties of Pd-P Catalysts in the Hydrogenation of Alkylanthraquinones. *Kinet. Catal.* **2019**, *60*, 808–817. [[CrossRef](#)]
29. Sunnardianto, G.K.; Bokas, G.; Hussein, A.; Walters, C.; Moulto, O.A.; Dey, P. Efficient hydrogen storage in defective graphene and its mechanical stability: A combined density functional theory and molecular dynamics simulation study. *Int. J. Hydrogen Energy* **2021**, *46*, 5485–5494. [[CrossRef](#)]
30. Kag, D.; Luhadiya, N.; Patil, N.D.; Kundalwal, S.I. Strain and defect engineering of graphene for hydrogen storage via atomistic modeling. *Int. J. Hydrogen Energy* **2021**, *46*, 22599–22610. [[CrossRef](#)]
31. López, M.J.; Cabria, I.; Alonso, J.A. Palladium Clusters Anchored on Graphene Vacancies and Their Effect on the Reversible Adsorption of Hydrogen. *J. Phys. Chem. C* **2014**, *118*, 5081–5090. [[CrossRef](#)]
32. Kim, G.; Jhi, S.-H.; Lim, S.; Park, N. Effect of vacancy defects in graphene on metal anchoring and hydrogen adsorption. *Appl. Phys. Lett.* **2009**, *94*, 173102. [[CrossRef](#)]
33. Kubas, J. Dihydrogen Complexes as Prototypes for the Coordination Chemistry of Saturated Molecules. *Proc. Natl. Acad. Sci. USA* **2007**, *104*, 6901–6907. [[CrossRef](#)] [[PubMed](#)]
34. Yoon, M.; Yang, S.; Wang, E.; Zhang, Z. Charged Fullerenes as High-Capacity Hydrogen Storage Media. *Nano Lett.* **2007**, *7*, 2578–2583. [[CrossRef](#)] [[PubMed](#)]

Disclaimer/Publisher’s Note: The statements, opinions and data contained in all publications are solely those of the individual author(s) and contributor(s) and not of MDPI and/or the editor(s). MDPI and/or the editor(s) disclaim responsibility for any injury to people or property resulting from any ideas, methods, instructions or products referred to in the content.